

Simple Approaches to Quality Large-Scale Tungsten Oxide Nanoneedles

Yi Zheng Jin,[†] Yan Qiu Zhu,^{*,‡} Raymond L. D. Whitby,[†] Nan Yao,[§] Renzhi Ma,^{||}
Paul C. P. Watts,[†] Harold W. Kroto, and David R. M. Walton[†]

School of Life Sciences, University of Sussex, Brighton BN1 9QJ, U.K., School of Mechanical, Materials, Manufacturing Engineering & Management, University of Nottingham, University Park, Nottingham NG7 2RD, U.K., Princeton Materials Institute, Princeton, New Jersey 08540, and Advanced Materials Laboratory, National Institute for Materials Science, Namiki 1-1, Tsukuba, Ibaraki 305-0044, Japan

Received: March 31, 2004; In Final Form: August 9, 2004

In this paper, a systematic study of large-scale production of highly crystalline $W_{18}O_{49}$ nanoneedles with high aspect ratios using a simple tungsten metal reacting with water at 800–1000 °C has been described. By altering the W source and other experimental conditions, we have generated $W_{18}O_{49}$ crystals with diverse morphologies, and needles with desired dimensions are achieved. The quality nanoneedles provide ideal samples for further property investigations. Possible growth mechanisms are discussed.

Introduction

Among the numerous transition metal semiconducting materials, the tungsten oxides WO_x ($x = 1-3$) which have been investigated extensively for their distinctive properties, are widely used in gas/humidity sensors, optical devices, electrochromic windows, catalysts, etc.^{1–5} The sodium-doped Na_xWO_3 ($x \sim 0.05$) is a high-temperature superconductor with $T_c \sim 90$ K.⁶ Monoclinic $W_{18}O_{49}$, which exhibits unique shear plane structural defects is of particular interest because of its potential applications in the nanoregime.^{7,8} For example, recent studies show that film consisting of $W_{18}O_{49}$ nanowire arrays exhibit excellent field emission properties.⁹ In particular, one-dimensional (1D) nanostructured $W_{18}O_{49}$ can be used as precursors of valuable 2H- WS_2 nanotube via a direct metathesis reaction with gaseous H_2/H_2S at ca. 900 °C.^{10–12} Thus the preparation of single-crystal, 1D $W_{18}O_{49}$ nanostructures on a large scale and with high purity is significantly important in the development of nanotechnology. Zhu et al. first reported the successful generation of $W_{18}O_{49}$ microtrees, obtained by heating a W foil covered with a quartz plate to 1600 °C in argon.¹³ The $W_{18}O_{49}$ micrometer-scaled trees are readily fragmented using ultrasonication into nanometer-scaled needles. Recently, a range of different techniques has been investigated to generate various types of 1D $W_{18}O_{49}$ nanostructures and understand the factors governing their morphology and control production. $W_{18}O_{49}$ nanowires have been prepared on metal tungsten tips by electrochemical etching, combined with subsequent treatment at 700 °C under an argon atmosphere.¹⁴ Controlled pyrolysis of a mixture of sodium tungstate and ammonium polyacrylate (APA) copolymer, followed by oxidation in CO_2 , leads exclusively to rod-shaped $W_{18}O_{49}$ crystals.¹⁵ By controlled removal of the surfactant from a mesolamellar tungsten oxide precursor at elevated temperature, $W_{18}O_{49}$ nanowires with diameters ranging from 10 to 50 nm are obtained.¹⁶ Soluble tungsten nanorods can be produced from $W(CO)_6$ using a solution-based

colloidal approach.¹⁷ Quasi-aligned $W_{18}O_{49}$ nanowires have been generated by a vapor-solid process in which tungsten foils are heated with infrared irradiation in a high-vacuum system.⁹ It is noteworthy that potassium-doped tungsten oxide nanowires (K:W:O = $\sim 0.54-0.6:1:\sim 3.4-3.6$) can be fabricated by simply heating W metal and KI in air.¹⁸ However, to date, high-purity generation of highly crystalline $W_{18}O_{49}$ has yet to be achieved, and an efficient process that is susceptible to facile scale-up is an important technical goal.

Tenne and co-workers have shown that WO_x ($x = 2.5-2.9$) whiskers, which can be subsequently used as inorganic fullerene-like WS_2 nanotube precursors, are formed when tungsten metal is vaporized in the presence of water vapor.¹⁰ In this paper, we have systematically studied the W– H_2O reaction in the 800–1000 °C temperature range. A simple route to large-scale, well-crystalline $W_{18}O_{49}$ nanoneedles with high aspect ratio is thus described. We find, by altering the W source and experimental conditions, $W_{18}O_{49}$ with diverse morphologies and sizes can be obtained. Possible growth mechanisms are discussed.

Experimental Section

A typical setup (experiment 1, Table 1) consists of a quartz boat containing 0.30 g of high-purity monocrystalline W powder (99.9%, 0.6–1 μm ; Aldrich Co.) placed in a quartz tube located in a conventional horizontal furnace. A 20 sccm (standard cubic centimeters per minute) argon flow was bubbled through a boiling water bath so that H_2O vapor was continuously transferred into the reaction zone whose temperature was raised to 800 °C. After 40 min of water vapor transfer, the furnace was allowed to cool to room temperature and ca. 0.33 g of a dark purple-blue powder was collected from the boat. At the downstream end of the tube a very small amount of yellow powder was deposited on the inner wall. A range of experiments (experiments 2–5, Table 1) was carried out to investigate how the various reaction parameters, including reaction time, temperature and H_2O pressure corresponding to argon flow, affect the final product.

All samples were characterized by several techniques: scanning electron microscopy (SEM, LEO-5000), X-ray diffraction (XRD, Siemens D-5000), transmission electron microscopy

* Corresponding author. E-mail: yanqiu.zhu@nottingham.ac.uk.

[†] University of Sussex.

[‡] University of Nottingham.

[§] Princeton Materials Institute.

^{||} National Institute for Materials Science.

TABLE 1: Parameters for W – H₂O Reactions

experiment/ sample	W source	temp/ °C	time/ min	argon flow/ sccm
1	monocrystalline W powder (99.9%, 0.6–1 μm ; Aldrich Co.)	800	40	20
2	monocrystalline W powder (99.9%, 0.6–1 μm ; Aldrich Co.)	800	20	20
3	monocrystalline W powder (99.9%, 0.6–1 μm ; Aldrich Co.)	800	120	20
4	monocrystalline W powder (99.9%, 0.6–1 μm ; Aldrich Co.)	1100	40	20
5	monocrystalline W powder (99.9%, 0.6–1 μm ; Aldrich Co.)	800	40	50
6	100 mesh W powder (99.95%, Aldrich Co.)	800	40	20
7	100 mesh W powder (99.95%, Aldrich Co.)	1000	60	20
8	W foil (0.05 mm thick, 99.9%, Aldrich Co.)	800	40	20
9	W wire (0.25 mm in diameter, 99.9%, Aldrich Co.)	800	40	20

(TEM, H7100), high-resolution transmission electron microscopy (HRTEM, CM200) and energy-dispersive X-ray spectroscopy (EDX). For the TEM samples, the powders were ultrasonically dispersed in acetone and dripped onto a holey carbon coated copper grid.

Results and Discussion

SEM observations indicate that the dark purple-blue powder mainly exhibits numerous straight nanoneedles, randomly orientated in the sample, with typical lengths of 10–20 μm , some of which even approach 100 μm (Figure 1a) and are ca. 20–400 nm in diameter, with the majority of diameter less than 200 nm. SEM and TEM observations reveal that individual needles possess uniform diameters throughout their lengths with an average aspect ratio of generally greater than 50. SEM observations also showed individual particles, ca. 0.5–1 μm in diameter, occasionally distributed throughout the sample. The detailed morphological and structural features were studied using HRTEM. Figure 1b shows a single nanoneedle with a diameter of ca. 70 nm that exhibits a well-defined lattice fringe (Figure 1c), implying that the crystal possesses a long-range order. The lattice fringe separations are 0.38 and 0.37 nm, respectively, which can be indexed as $\{010\}$ and $\{103\}$ of a monoclinic $\text{W}_{18}\text{O}_{49}$ crystal, according to JCPDS card no. 36-0101 and in agreement with electron diffraction (ED) results (Figure 1d). The growth direction of the nanoneedle is along the $[010]$ axis, which is the close-packed plane of the crystalline monoclinic $\text{W}_{18}\text{O}_{49}$. The preferential growth along the $[010]$ direction results in the highest peak intensity in the XRD pattern (Figure 2). The ED image of the nanoneedle shows streaking around diffraction spots, as well as distinct satellite spots, revealing the existence of stacking faults formed in the direction normal to the $[010]$ direction. Such nanoneedle crystal features are consistent with previous reports.^{9,16} SEM and XRD examinations of the yellow powders, which were deposited on the inner wall

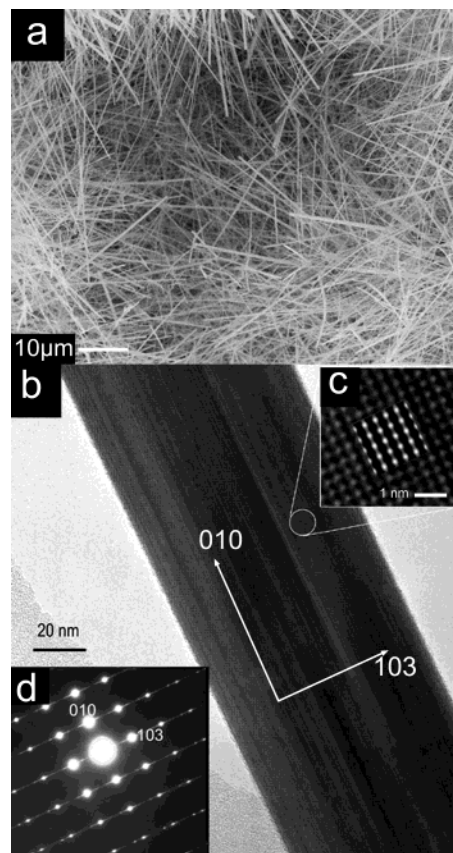


Figure 1. (a) SEM image of $\text{W}_{18}\text{O}_{49}$ nanoneedles. (b) HRTEM image of one individual $\text{W}_{18}\text{O}_{49}$ nanoneedle. (c) Enlarged HRTEM pattern with an inset of HRTEM simulation pattern. (d) ED pattern of the nanoneedle.

of the quartz tube, revealed that they are faceted WO_3 crystals (JCPDS card no. 24-0747), ca. tens of microns in size. High-resolution simulation of the HRTEM image was performed on a Silicon Graphics computer using Cerius² software. As the image were taken from a CM200 HRTEM, the following parameters were used: energy = 200 kV, spherical aberration coefficient, $C_s = 2.70$ mm, defocus = -822.9 Å, beam divergence = 0.30 mrad, defocus spread = 250 Å. The resulting simulated TEM image provides an excellent match to that of the $\text{W}_{18}\text{O}_{49}$ needle (Figure 1c).

The XRD profiles for W and $\text{W}_{18}\text{O}_{49}$ were simulated (Figure 2a,b, respectively) and compared to that of sample 1 (Figure 2c). The XRD profile matches well with that of bulk monoclinic $\text{W}_{18}\text{O}_{49}$ and a number of low intensity peaks corresponding to residual W metal can be identified (asterisked peaks in 2c). Consistent with general features of nanomaterials, the overall diffraction intensities appear to be weak, and a slight broadening feature is observable. From the detailed study, experiments 1–5, we found that by shortening the reaction time to 20 min, we were able to detect an intermediate product. Similarly, we simulated XRD profiles for W and WO_2 (Figure 3a,b, respectively) and then compared them with the XRD spectrum obtained from experiment 2. We find that this sample contains a number of reflections that correspond to WO_2 (JCPDS card no. 32-1393) and residual W. This suggests that monoclinic WO_2 may be an intermediate phase in the formation of $\text{W}_{18}\text{O}_{49}$ from W. This is consistent with the phase transformation sequence: $\text{W} \rightarrow \text{WO}_2 \rightarrow \text{W}_{18}\text{O}_{49}/\text{W}_{20}\text{O}_{48} \rightarrow \text{WO}_3$, believed to occur at 800 °C.¹⁹ Moreover, the onset of $\text{W}_{18}\text{O}_{49}$ formation is apparent from the presence of its $\{010\}$ peak (Figure 2c, asterisked peak).

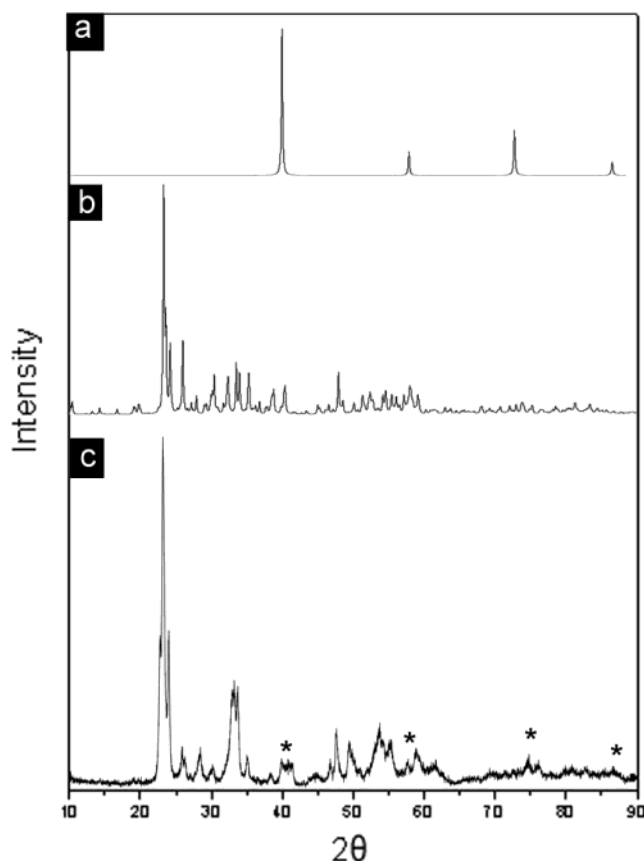


Figure 2. XRD profiles of (a) W particle simulation, (b) $W_{18}O_{49}$ crystal simulation, (c) sample 1. The peak marked (*) corresponds to W.

It should be noted that identification of $W_{20}O_{48}$ in sample 1 is difficult as there are no related peaks observed in the XRD pattern, possibly due to their low intensity reflections (if present) being overlapped by those of W and $W_{18}O_{49}$. We also surmise that WO_2 reflections were not distinguishable in the final XRD result, for sample 1, due to the low quantities anticipated as being present as thin outer layers on the particles during the initial steps of W oxidation. We found that when oxidation is prolonged beyond 40 min, Sample 1 continues its transformation to yellow powders and after 2 h (experiment 3) oxidation is completed, resulting in pure WO_3 powders. We also found that by increasing the temperature above 1100 °C, yellow faceted WO_3 crystals (experiment 4) are solely formed. Furthermore, by increasing the argon flow rate, which is associated with raising the partial pressure of H_2O , the production of yellow WO_3 powders predominates (experiment 5).

The formation of large grains or agglomerates of metal W during the reduction of yellow WO_3 powders in a H_2 stream aroused interest decades ago.²⁰ Early studies demonstrated that the formation of WO_x clusters with $W_{18}O_{49}$ microwhiskers sprouting from parent cores is the key stage in this process.^{21,22} The initial reduction of WO_3 results in large $W_{18}O_{49}$ whisker clusters that could decompose to form agglomerates of WO_2 containing several primary crystals.^{21,22} The presence of H_2O vapor, whether it is a product of the H_2 reduction or deliberately added to the reductive vapor, could greatly promote the growth rate of the $W_{18}O_{49}$ whiskers.^{20,21,23} The formation of a volatile tungsten compound $WO_2 \cdot nH_2O$ (or a similar hydrate species of tungsten suboxides) has been linked to the controlling factor in this process.^{21,24} The final reduction of WO_2 to W is achieved without any morphological change. It has also been noted that the diameters of $W_{18}O_{49}$ microwhiskers, arising from the WO_x

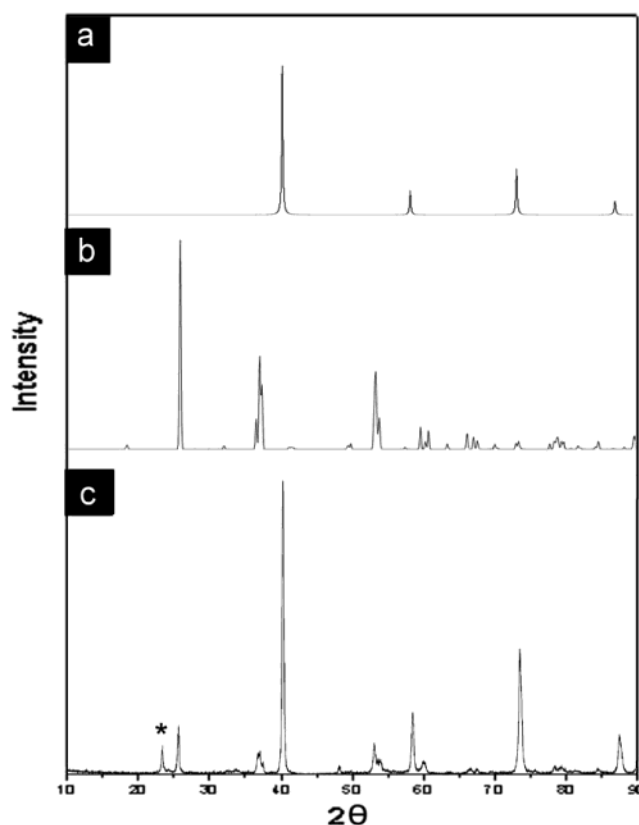
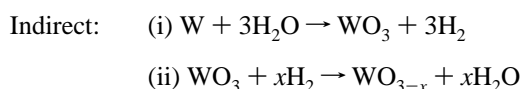
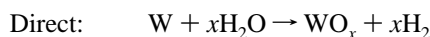


Figure 3. XRD profiles of (a) W particle simulation, (b) WO_2 crystal simulation, (c) sample 2. The peak marked (*) corresponds to $W_{18}O_{49}$.

clusters, are determined primarily by the size of the WO_3 particles in the initial reduction.²¹ Tenne et al. also showed that H_2O is essential for the synthesis of the WO_x ($2.5 < x \leq 2.9$) nanowhiskers and nanoparticles via the W filament oxidation.¹⁰ The following direct and indirect reaction schemes are postulated for the formation of WO_x ($2.5 < x \leq 2.9$):



We surmise that the direct mechanism is operating in our experiment based on the following. The XRD results indicate WO_2 is formed in the initial stages of oxidation as the intermediate toward generation of the $W_{18}O_{49}$ crystals. Although the possibility that reduction of local crystal domains, close to the liberation site of hydrogen, cannot be excluded, the bulk of the crystals have been characterized as W and WO_2 in the initial stages of oxidation and no reflections for WO_3 are observed in the XRD spectra. It is thus reasonable to conclude that the conditions employed in a gas-flow reactor do not favor reaction of H_2 and subsequent reduction of a formed bulk WO_3 crystal to a suboxide species. Based on the direct mechanism for W oxidation toward $W_{18}O_{49}$, it is reasonable to suppose the following growth mechanism:

(1) WO_2 layers are formed on W particle surfaces at the incipient stages.

(2) A volatile tungsten compound $WO_2 \cdot nH_2O$ (or a similar hydrate species of tungsten suboxides) then forms on the outer WO_2 surface, and in the presence of water vapor permanent hydrolysis breaks up the W–O–W chains, in the WO_2 layers, allowing the formation and nucleation of localized $W_{18}O_{49}$

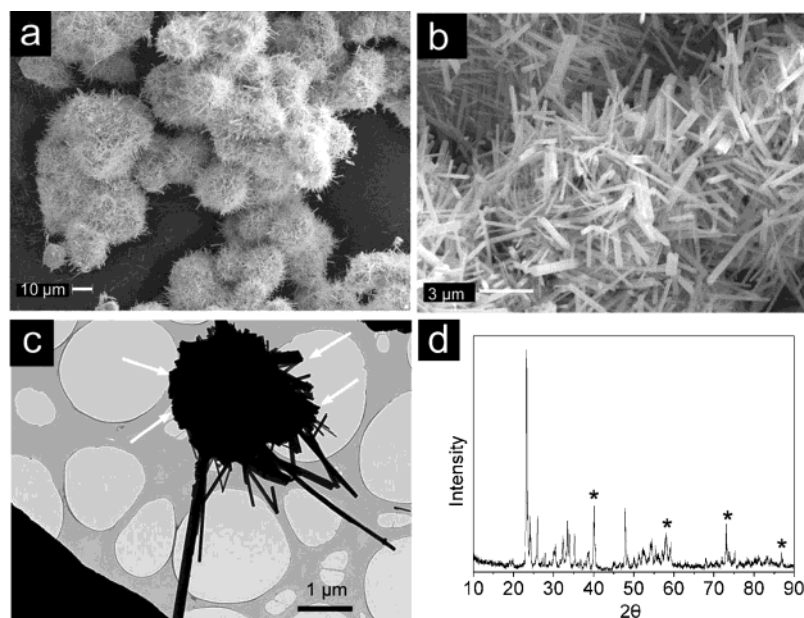


Figure 4. (a) SEM image of sample 6. (b) High-magnification SEM image. (c) TEM image of sample 6. (d) XRD pattern of sample 6. The peak marked (*) corresponds to W.

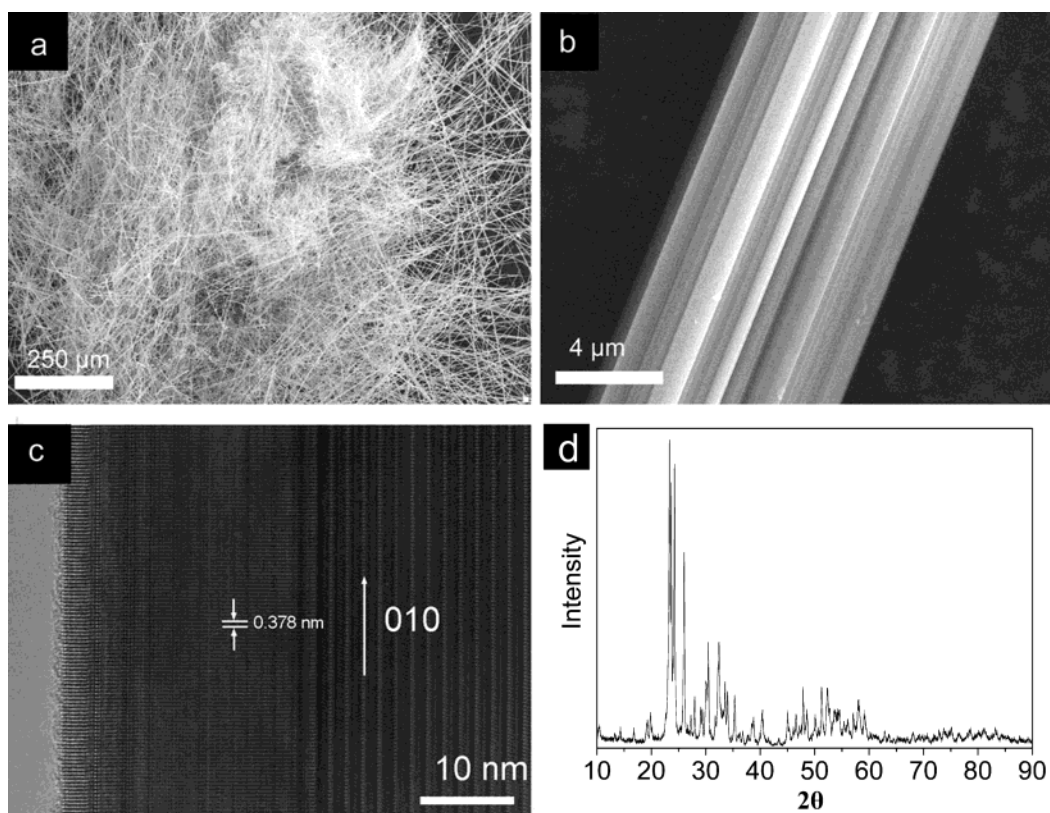


Figure 5. (a) SEM image of $W_{18}O_{49}$ microbundles. (b) SEM image of one individual $W_{18}O_{49}$ microbundle. (c) HRTEM image of a $W_{18}O_{49}$ microbundle. (d) XRD pattern of sample 7.

crystals. The nanoneedles are found to grow along the b -axis of the $W_{18}O_{49}$ monoclinic unit cell, with the $\{010\}$ as the growth plane. Because the $W_{18}O_{49}$ lattice is built up of WO_6 octahedra coupled with each other in an intricate way by sharing corners and edges,²⁵ the fastest growth rate is probably achieved by linking these octahedra to form linear rows along the b -axis.

(3) Upon further oxidation, the nanoneedles can be converted into WO_3 particles and the whole oxidation process $W \rightarrow WO_2 \rightarrow W_{18}O_{49}/W_{20}O_{48} \rightarrow WO_3$ is achieved.

Having examined various parameters and characterized the species obtained in the oxidation of tungsten, it is evident that the reaction can be optimized (and terminated) to yield the maximum amount of $W_{18}O_{49}$ nanoneedles. The best we have obtained so far yields ca. 80% of $W_{18}O_{49}$ nanoneedles. As suggested in the WO_3 reduction process, the diameters of $W_{18}O_{49}$ microwhiskers extending from the WO_x clusters are determined mainly by the size of parent WO_3 particles,²¹ indicating a template effect is operating. Here we explored the

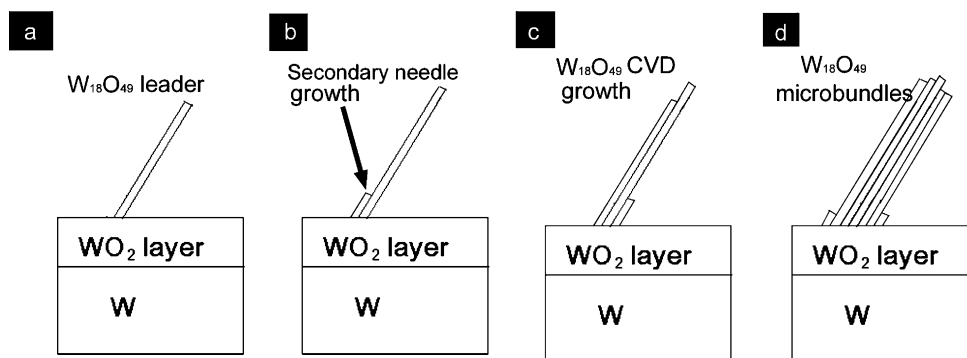


Figure 6. Secondary needle CVD growth model: (a) formation of WO_2 layer and $\text{W}_{18}\text{O}_{49}$ leader crystal; (b) secondary needle growth parallel to the leader $\text{W}_{18}\text{O}_{49}$ needle; (c) CVD growth of $\text{W}_{18}\text{O}_{49}$ needles with a selective growth rate; (d) formation of $\text{W}_{18}\text{O}_{49}$ microbundle by continuous growth of secondary needles.

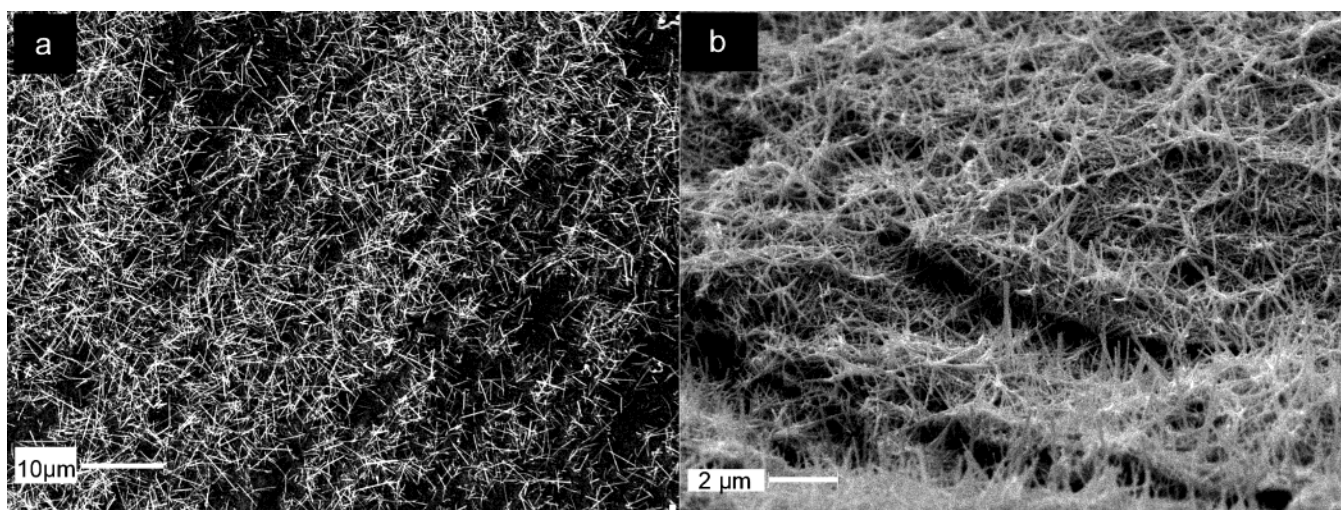


Figure 7. SEM images of (a) sample 8 and (b) sample 9.

W precursor–needle oxide size relationship during oxidation. On the substitution of the $1\text{ }\mu\text{m}$ W powder for a 100 mesh powder, while other conditions are kept constant (experiment 6), the SEM image (Figure 4a) reveals the sample consists mainly of particles with a spiky-ball morphology. Numerous individual needles/rods sprout from the parent particles, bearing morphologies similar to those previously reported $\text{W}_{18}\text{O}_{49}$ microwhiskers formed during WO_3 reduction.^{21,22} A detailed SEM image in Figure 4b shows that the dimensions of the resulting needles/rods are significantly increased (ca. $10\text{--}20\text{ }\mu\text{m}$ long and ca. $0.5\text{--}1.0\text{ }\mu\text{m}$ in diameter) compared with those in sample 1. This is consistent with the direct relationship between precursor particle size and the resulting needles/rods diameter. The numerous WO_x spiky-balls exhibit some breakage of the whiskers (arrowed, Figure 4c) which occurs during sonication step in the TEM preparation. XRD analysis reveals the presence of $\text{W}_{18}\text{O}_{49}$ as well as residual W (Figure 4d, asterisked peak). The $\text{W}/\text{W}_{18}\text{O}_{49}$ peak intensity ratio is significantly increased compared with sample 1, indicating a greater amount of unreacted W.

We believe that the high temperature, $1000\text{ }^\circ\text{C}$, appears to favor the formation of $\text{W}_{18}\text{O}_{49}$ crystals during a CVD process involving $\text{WO}_2 \cdot n\text{H}_2\text{O}$ (or a similar hydrate species of tungsten suboxides). When the 100 mesh W powder is used as the precursor and the experimental parameters optimized (experiment 7), complete consumption of the W metal occurs and this leads to numerous microbundles in the cotton-like product. SEM (Figure 5a) observations show almost 100% purity of the microbundles comprising individual parallel-aligned $\text{W}_{18}\text{O}_{49}$

platelike nanoneedles (Figure 5b) in sample 7. These bundles can be several hundred microns long, sometimes up to 1 mm in length. HRTEM analyses show that the growth direction of these needles is also along the $[010]$ direction (Figure 5c). XRD analysis (Figure 5d) reveals that the sample is pure $\text{W}_{18}\text{O}_{49}$ where no W peaks are observed. Due to the predominating $\text{W}_{18}\text{O}_{49}$ crystals, it is difficult to ascertain whether WO_2 or $\text{W}_{20}\text{O}_{58}$ is present in the sample. Along with the $\text{W} \rightarrow \text{WO}_2 \rightarrow \text{W}_{18}\text{O}_{49}/\text{W}_{20}\text{O}_{58}$ sequence, a stepwise secondary needle CVD growth mechanism (Figure 6) is thus feasible, similar to that reported by Pfeifer et al.²⁴ In the initial reaction stage, rapid growth of a “leader crystal” propagates away from the WO_2 layer under “wet conditions” (Figure 6a). The presence of $\text{WO}_2 \cdot n\text{H}_2\text{O}$ in the gas phase would facilitate growth of subsequent needles parallel to the leader whisker (Figure 6b). A CVD process for $\text{W}_{18}\text{O}_{49}$ formation on the entire surface of this leading crystal is believed to play a definite role in the intergrowth of individual needles. Vapor grown materials fill in empty channels among the primary crystals and the later grown needles by a high selective growth rate (Figure 6c). Continuous growths of the secondary needles lead to the final $\text{W}_{18}\text{O}_{49}$ microbundles (Figure 6d) projecting away from the W particle surface, giving rise to the spiky-ball morphology. At the same time, some $\text{WO}_2\text{--H}_2\text{O}$ vapor will be conveyed by the argon flow and nucleated at a location away from quartz boat, thus leading to some of the product deposited on the far end of the quartz tube wall. This phenomenon appears to be temperature dependent, for experiments conducted at $800\text{ }^\circ\text{C}$ the majority of the product was converted within the boat, and

for experiments carried out at higher temperature, 1200 °C, 20–30% of the product formed outside of the boat. Further study regarding the kinetics of the nanoneedle growth, which involves the temperature, Ar gas flow rate, reaction time, etc., is in progress.

To expand this reaction further, experiments were carried out with a range of 2D W surfaces: 0.05 mm thick W foils and W wires with 0.25 mm in diameter (experiments 8 and 9, respectively). By the ends of the experiments, the surfaces of the foils and wires all became purple/blue. The SEM images of samples 8 and 9 are displayed in Figure 7a,b, respectively. The W foil surfaces were covered by randomly orientated nanoneedles, whereas the wire surfaces were covered by nanoneedle bushes. We surmise that the convex nature of the wire surface to provide numerous sites for WO₂ nucleation leads to the growth of W₁₈O₄₉ bushes, comparable with the uniform surface of a planar substrate.

Conclusions

The study has shown how tungsten oxide nanoneedles of high quality can be produced on a large scale via the reactions between W powder and H₂O vapor. The resulting nanoneedles are single crystals, which exhibit a high length–aspect ratio. By altering the size of the raw materials and varying the reaction parameters, we have obtained various W₁₈O₄₉ structures with different sizes and morphologies, including W₁₈O₄₉ clusters with whiskers sprouting from the parent crystals and randomly orientated W₁₈O₄₉ microbundles consisting of individual nanoneedles. A direct mechanism, which mainly involves the formation of WO₂ intermediate phase, is described to demonstrate the nanoneedle growth, and a secondary needle CVD growth mechanism is applied to the bundles formation. The procedures presented in this report on W₁₈O₄₉ nanoneedles production are simple, efficient, and easy to scale up.

Acknowledgment. We thank the EPSRC for financial support. We are grateful to J. Thorpe and D. Randall (Sussex)

for assistance with TEM and SEM facilities and Dr. Chao Gao for the helpful discussion.

References and Notes

- (1) Solis, J. L.; Saukko, S.; Kish, L.; Granqvist, C. G.; Lantto, V. *Thin Solid Films* **2001**, 391, 255.
- (2) Li, Y. J.; Tsai, P. P. *Solid State Ion.* **1996**, 86–8, 1001.
- (3) Solis, J. L.; Hoel, A.; Lantto, V.; Granqvist, C. G. *J. Appl. Phys.* **2001**, 89, 2727.
- (4) Santato, C.; Odziemkowski, M.; Ulmann, M.; Augustynski, J. *J. Am. Chem. Soc.* **2001**, 123, 10639.
- (5) Alvarez-Merino, M. A.; Carrasco-Marin, F.; Fierro, J. L. G.; Moreno-Castilla, C. *J. Catal.* **2000**, 192, 363.
- (6) Shengelaya, A.; Reich, S.; Tsabba, Y.; Muller, K. A. *Eur. Phys. J. B* **1999**, 12, 13.
- (7) Sahle, W. J. *Solid State Chem.* **1982**, 45, 334.
- (8) Lou, X. W.; Zeng, H. C. *Inorg. Chem.* **2003**, 42, 6169.
- (9) Li, Y. B.; Bando, Y.; Golberg, D. *Adv. Mater.* **2003**, 15, 1294.
- (10) Rothschild, A.; Sloan, J.; Tenne, R. *J. Am. Chem. Soc.* **2000**, 122, 5169.
- (11) Zhu, Y. Q.; Hsu, W. K.; Grobert, N.; Chang, B. H.; Terrones, M.; Terrones, H.; Kroto, H. W.; Walton, D. R. M.; Wei, B. Q. *Chem. Mater.* **2000**, 12, 1190.
- (12) Homyonfer, M.; Alpers, B.; Rosenberg, Y.; Sapir, L.; Cohen, S. R.; Hodes, G.; Tenne, R. *J. Am. Chem. Soc.* **1997**, 119, 2693.
- (13) Zhu, Y. Q.; Hu, W. B.; Hsu, W. K.; Terrones, M.; Grobert, N.; Hare, J. P.; Kroto, H. W.; Walton, D. R. M.; Terrones, H. *Chem. Phys. Lett.* **1999**, 309, 327.
- (14) Gu, G.; Zheng, B.; Han, W. Q.; Roth, S.; Liu, J. *Nano Lett.* **2002**, 2, 849.
- (15) Hudson, M. J.; Peckett, J. W.; Harris, P. J. F. *J. Mater. Chem.* **2003**, 13, 445.
- (16) Li, X. L.; Liu, J. F.; Li, Y. D. *Inorg. Chem.* **2003**, 42, 921.
- (17) Lee, K.; Seo, W. S.; Park, J. T. *J. Am. Chem. Soc.* **2003**, 125, 3408.
- (18) Qi, H.; Wang, C. Y.; Liu, J. *Adv. Mater.* **2003**, 15, 411.
- (19) St. Pierre, G. R.; Ebihara, W. T.; Pool, M. J.; Speiser, R. *Trans. Met. Soc. AIME* **1962**, 230, 259.
- (20) Millner, T.; Neugebauer, J. *Nature* **1949**, 163, 601.
- (21) Sarin, V. K. *J. Mater. Sci.* **1975**, 10, 593.
- (22) Sahle, W. J. *Solid State Chem.* **1982**, 45, 324.
- (23) Berglund, S.; Sahle, W. J. *Solid State Chem.* **1981**, 36, 66.
- (24) Pfeifer, J.; Badaljan, E.; TekulaBuxbaum, P.; Kovacs, T.; Geszti, O.; Toth, A. L.; Lunk, H. J. *J. Cryst. Growth* **1996**, 169, 727.
- (25) Viswanathan, K.; Brandt, K.; Salje, E. J. *Solid State Chem.* **1981**, 36, 45.